

A simple channelling model for HREM contrast transfer under dynamical conditions

W. SINKLER* & L. D. MARKS

*Northwestern University, Department of Materials Science and Engineering, Evanston,
IL 60208-3108, U.S.A.*

Key words. Dynamical diffraction theory, electron channelling, HREM imaging theory.

Summary

The application of electron channelling theory to dynamical exit wave calculations is briefly reviewed, and a comparison of channelling results with full dynamical calculations is presented. The channelling expression to the exit wave is combined with conventional imaging theory, and it is shown that a simple expression can be obtained for a dynamical contrast transfer function (D-CTF), which incorporates imaging aberrations and thickness-dependent dynamical scattering effects. The D-CTF can provide detailed insight into HREM images of a mixed cation oxide at thicknesses up to 200 Å, whereby an approximate correction for non-linear effects is utilized in the larger thickness regime.

1. Introduction

The possibility of using numerical calculations to accurately explain the contrast in high-resolution microscope images from thin samples has existed for many years. In its simplest form, image aberrations introduced by the microscope optics can be accounted for using the linear theory first developed by Scherzer (1949). The dynamical interaction between an incident plane wave and the sample can be modelled by a number of techniques, most commonly via multislice simulations (Cowley & Moodie, 1957). Additional techniques for calculating dynamical diffraction, such as the Sturkey scattering matrix formulation (Sturkey, 1962), the Bloch wave theory of Howie & Whelan (1961) or the real space method of Van Dyck & Coene (1984), all build from the same theoretical framework provided by Bethe (1928), and give results which are essentially in agreement for a given set of diffraction conditions. Thus, the theory of

electron diffraction is well established in its main aspects, and a strong consensus exists.

In spite of the development of a consistent body of electron diffraction and imaging theory, the complex nature of the calculations, especially for electron diffraction, tends to obscure essential qualitative features of the diffraction and imaging processes for the microscopist. As a simplification, one alternative to complete dynamical calculations is kinematical theory. The kinematical theory is however, valid only for thicknesses which are at the limit of what is obtainable with real specimens, and it is thus inapplicable in most cases. Two-beam dynamical theory, while instructive for general features of dynamical interaction, and for certain off-axis imaging conditions, has little bearing on zone-axis imaging.

In contrast to the above, electron channelling theory (Berry, 1971; Gemmell, 1974; Kambe *et al.* 1974; Tamura & Ohtsuki, 1974; Fujimoto, 1978; Kambe, 1982; Ohtsuki, 1983; Marks, 1985; Van Dyck, 1985; Van Dyck & Op de Beeck, 1996; Sinkler *et al.* 1998a) is capable of providing real insight into on-zone diffraction, in a framework which is analytical and tractable. The theory has existed for nearly 30 years, but is not widely represented in current literature, and is particularly underrepresented in pedagogical literature. However, it has significant value in elucidating many aspects of dynamical interaction. For example, it provides a full explanation of recent work in direct methods, in which it was found that use of strongly dynamical electron diffraction data can lead to a sensitivity toward light atoms (Sinkler *et al.*, 1998a; Sinkler *et al.*, 1998b; Sinkler & Marks, 1999). It has also been applied to image formation in high resolution microscopy (HREM) (Van Dyck, 1985). Its relatively simple analytical form makes it readily adaptable to straightforward approximate treatment of topics such as diffraction from a wedge-shaped crystal (Sinkler & Marks, 1999), and other themes which may be cumbersome to treat numerically. In addition, it may have potential for use as a first step in refinements, as it allows dynamical effects

Correspondence to: W. Sinkler. Tel: +1 208-533-7724; fax: +1 208-533-7863;
e-mail: wharton.sinkler@anlw.anl.gov.

* Present address: Argonne National Lab West, PO Box 2528, Idaho Falls,
ID 83403, U.S.A.

to be accounted for in a first-order approximation (beyond kinematical) while providing an algorithm which is vastly simpler and faster to compute than a full dynamical calculation.

In this paper, standard linear and non-linear imaging theory will be applied to the simple analytical expression for the exit wave, which is obtained from electron channelling theory. The primary goal will be to establish the viability of using channelling theory to develop an analytical description of the principal features of dynamical HREM images, i.e. images at sample thicknesses which are beyond the validity of the kinematical approximation. The applicability of the analytical theory based on channelling will necessarily be limited by the channelling approximations to the case of zone-axis imaging in which well-separated atomic columns are aligned parallel to the electron beam. Multislice and the other numerical methods will remain the methods of choice when it is necessary to calculate images to the highest possible accuracy. Nevertheless, it will be shown that channelling theory and standard imaging theory can be used to fill the significant gap between the well-known kinematical approximation, and accurate but purely numerical methods of image calculation. Section II of this article presents a brief review of the channelling theory used in the remainder of the article. No detailed derivation will be given, but the aim will be to develop a single simple expression, with a minimum number of parameters, which nevertheless provides a fair approximation to a many-beam diffracted wave for samples consisting of well-separated columns along the beam direction. In Section III, the analytical channelling expression will be compared with multislice simulations of the complex exit wave $\psi(\mathbf{r})$ for a real crystal $(\text{Ga},\text{In})_2\text{SnO}_5$. Section IV presents an application of linear and non-linear imaging theory to the exit wave expression obtained from the channelling theory. The result is a modified CTF, including both thickness-dependent and imaging effects in a simple expression. The modified CTF can provide detailed insight into HREM images at thicknesses for which the standard kinematical CTF is not applicable. This is demonstrated via interpretations of simulated HREM images of the $(\text{Ga},\text{In})_2\text{SnO}_5$ mixed oxide structure for thicknesses to nearly 200 Å.

2. Electron channelling theory

The development of electron channelling theory began in the early seventies with the work of Berry (1971) and builds on the earlier classical theory for ion channelling due to Lindhard (1964). Electron channelling has received significant additional contributions from a number of researchers referenced above. The central approximation is the neglect of all scattering contributions outside of the zero order Laue zone. In this sense electron channelling is a high-energy approximation, suitable for situations in which

the incident beam is along a major zone axis, so that the contribution of first and higher order Laue zones is minimized. Derivations along several different lines may be found in the literature (Berry, 1971; Kambe *et al.*, 1974; Van Dyck & Op de Beeck, 1996), and will not be repeated here. However, the central result is a description of the electron exit wave at the bottom surface of the specimen as (Van Dyck & Op de Beeck, 1996):

$$\psi(\mathbf{R}, z) = 1 + \sum_n C_n \phi_n(\mathbf{R}) \times \left\{ \exp \left(-i\pi \frac{E_n}{E_0} kz \right) - 1 \right\} \quad (1)$$

in which $\mathbf{R} = (x, y)$ is a two-dimensional vector perpendicular to the incident beam direction. The $\phi_n(\mathbf{R})$ and E_n are eigenfunctions and energy eigenvalues of a two-dimensional Schrödinger equation for an electron in the specimen projected potential. The channelling approximation significantly simplifies the more general Bloch wave solution, expressing it as a superposition of a set of two-dimensional functions ϕ_n , each modulated by a characteristic oscillation along the z -direction.

A significant further simplification which can be combined with the channelling formalism is the atomic column approximation (Van Dyck, 1985). The wavefunction for the entire crystal is thereby approximated as a superposition of individual atomic bound state wavefunctions, i.e.

$$\psi(\mathbf{R}, z) = 1 + \sum_i C_i \Phi_i(\mathbf{R} - \mathbf{R}_i) \left(\exp \left(-i\pi \frac{E_i}{E_0} kz \right) - 1 \right) \quad (2)$$

where now the sum is over the i atomic positions, and Φ_i is the lowest-energy atomic bound state for atom i . This lowest-energy state is a centrally peaked radially symmetric function which is the two-dimensional analogue of an atomic 1 s state. Validity of this approximation requires that the potential consist of well-separated atomic columns, so that the only significant bound states are those of the individual atomic columns (as opposed to more complex states involving more than a single atomic column potential). A reasonable approximation to this deepest bound state may be obtained by considering the case of a potential containing a single atomic column, and setting this equal to the expression for a weak phase-object as z approaches zero (Sinkler *et al.* 1998a). From this, one obtains:

$$C_i \Phi_i(\mathbf{R}) = \frac{V(\mathbf{R})}{E_i} \quad (3)$$

and the final approximate expression for the dynamical exit wave is therefore:

$$\psi(\mathbf{R}, z) = 1 + \sum_i \frac{V_i(\mathbf{R} - \mathbf{R}_i)}{E_i} \left(\exp \left(-i\pi \frac{E_i}{E_0} kz \right) - 1 \right) \quad (4)$$

In this expression for the exit wave, the only unknown parameters are the 1 s bound state energies E_i , of which there is one for each unique column in the projected

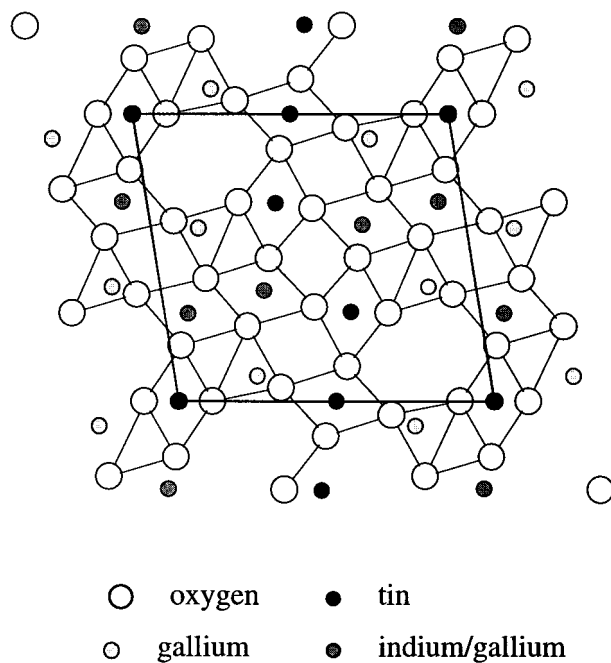


Fig. 1. Ball-and-stick model of $(\text{Ga},\text{In})_2\text{SnO}_5$, viewed in *b*-axis projection.

structure. The wave has a particularly simple form in this expression: it consists of discrete maxima, in form identical to the atomic potentials $V_i(\mathbf{R})$, which oscillate in both amplitude and phase as a function of thickness. The form of the oscillation is given by the term in parentheses which describes a unit circle centred at $(-1,0)$ in the complex plane. In the following section, the ability of Eq. (4) adequately to describe the exit wave for a real crystal consisting of well-separated atomic columns along the beam will be investigated using comparisons with multislice simulations for $(\text{Ga},\text{In})_2\text{SnO}_5$.

3. Comparison of channelling approximation with multislice simulation

Figure 1 shows a ball-and-stick model of $(\text{Ga},\text{In})_2\text{SnO}_5$, which was recently solved in the course of an investigation

Table 1. Energy eigenvalues (all values in eV). Calculation for isolated atomic column with interatomic distance of 3.163 \AA , and from multislice for the $(\text{Ga},\text{In})_2\text{SnO}_5$, [010] projection.

Atom	Eigenvalue (isolated atom)	Eigenvalue (multislice)
Oxygen	-15.486	-28
Gallium	-101.462	-128
Gallium/indium (50%)	-144.204	-194
Tin	-193.817	-246

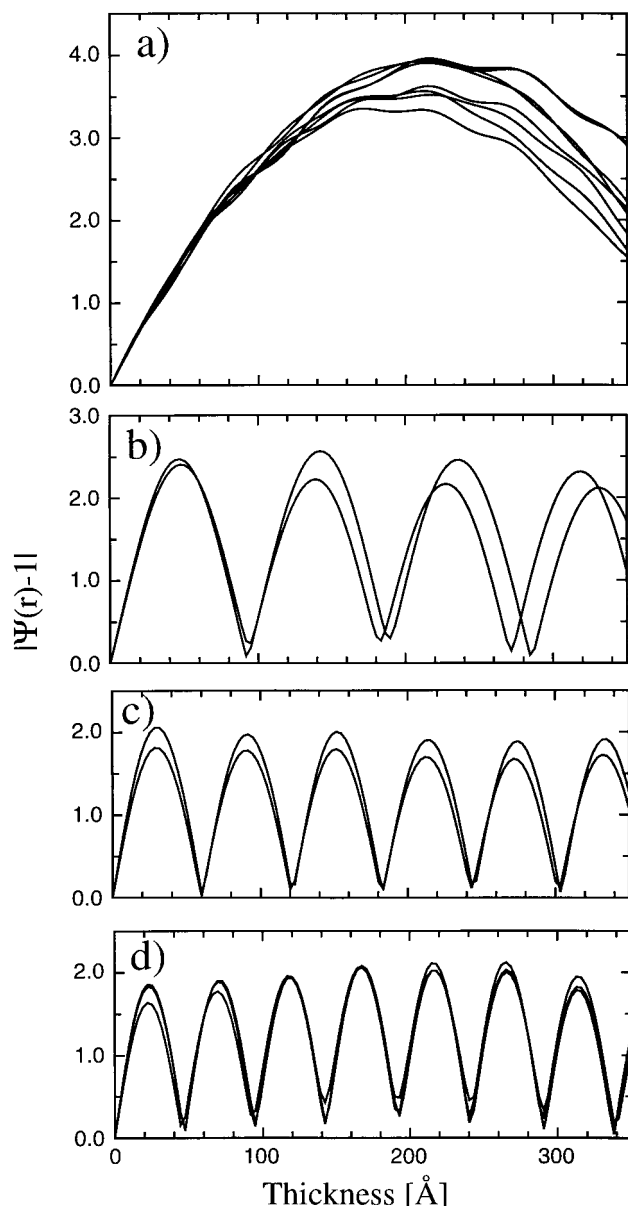


Fig. 2. Amplitudes of $|\psi(r)-1|$ at the centres of atomic columns for all unique atoms in the $(\text{Ga},\text{In})_2\text{SnO}_5$ structure [010] projection. (a) oxygen, (b) gallium, (c) gallium/indium, (d) tin. Curves calculated with multislice, using Debye–Waller factors $B=0.3 \text{ \AA}^2$ (metal atoms) and $B=0.5 \text{ \AA}^{22}$ (oxygens). The multiple curves plotted are for the different unique atoms in the unit cell.

of the $\text{Ga}_2\text{O}_3\text{--In}_2\text{O}_3\text{--SnO}_2$ system for transparent conducting oxides (Edwards & Mason, 1998). The structure in *b*-axis orientation is particularly suitable for treatment using the channelling theory, as it consists along this direction of close-packed atomic columns, which are well separated in projection. It is not to be expected that the approximation given by Eq. (4) will be valid for more general structures and orientations in which there is significant

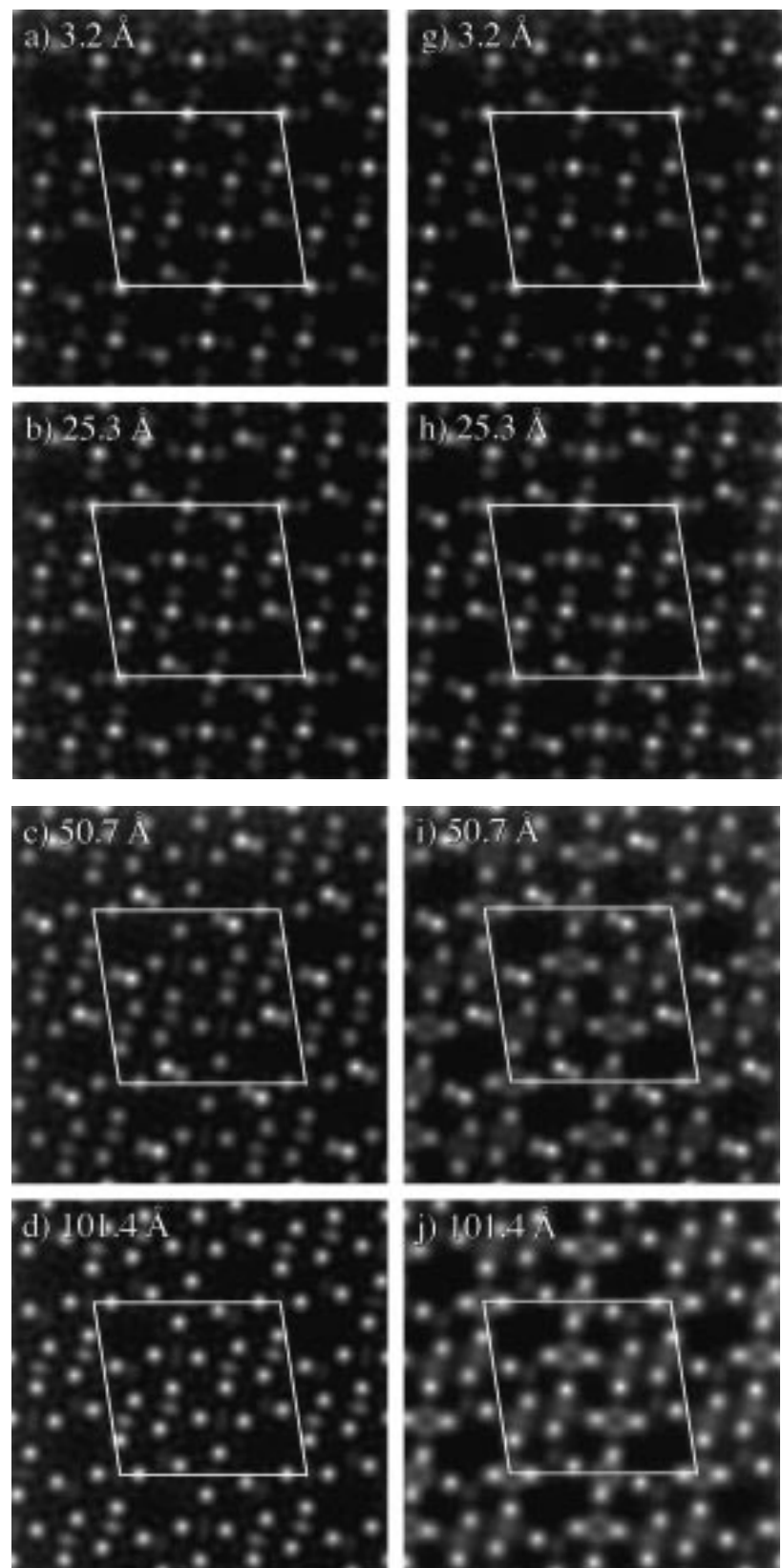


Fig. 3. Comparison of exit waves $|\psi(\mathbf{r}) - 1|$ for $(\text{Ga}, \text{In})_2\text{SnO}_5$ calculated using Eq. (5) (a-f) and multislice (g-l), at the thicknesses noted.

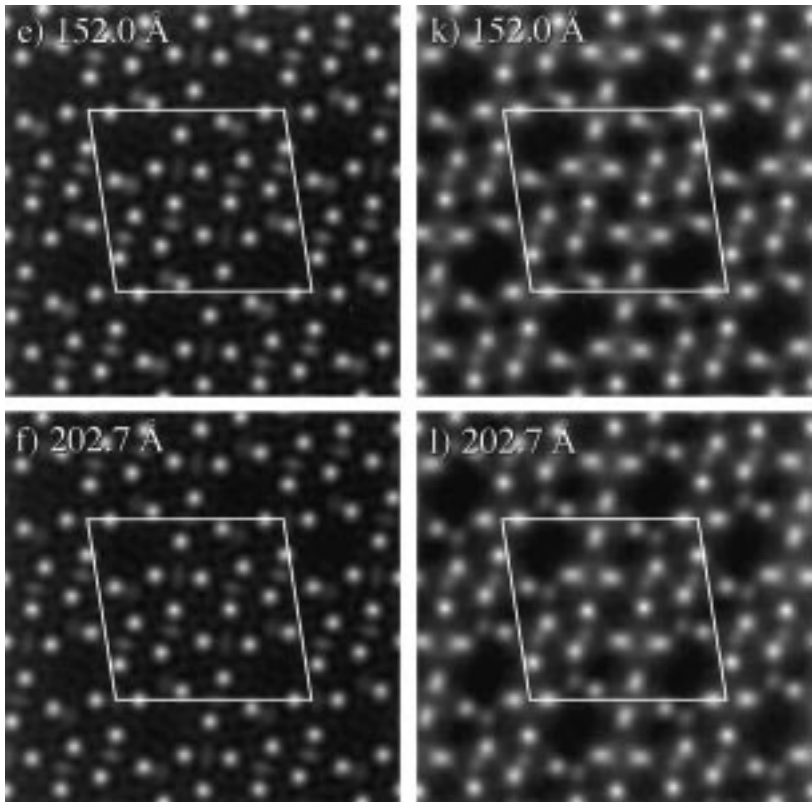


Fig. 3. Continued.

overlap of neighbouring atoms in the projected potential (Sinkler & Marks, 1999). However, many electron microscopy techniques, particularly HREM imaging, tend to be most useful for well-separated atomic columns along the beam direction. Therefore, conclusions drawn from this case will nonetheless be applicable to a large number of cases in which HREM imaging is most effective.

The energy eigenvalues E_i may be obtained by solving the Schrödinger equation for an isolated atomic column potential, and the result of such a calculation is shown in Table 1 for all atom types in the $(\text{Ga},\text{In})_2\text{SnO}_5$ structure. However, these eigenvalues differ somewhat, due to slight overlap of potentials, from those obtained empirically from multislice calculations. For example, under the assumption that the atomic potentials are well separated, the function $|\psi(\mathbf{R},z)-1|$ may be written using Eq. (4) as:

$$|\psi(\mathbf{R},z)-1| = \sum_i 2 \left| \frac{V_i(\mathbf{R} - \mathbf{R}_i)}{E_i} \right| \times \left| \sin \left(\pi \frac{E_i}{2E_0} kz \right) \right| \quad (5)$$

Near to an atomic column, the function $|\psi(\mathbf{r},z)-1|$ therefore oscillates with depth with a wavelength given by $2E_0\lambda/|E_i|$, as shown in Fig. 2 based on multislice simulations. Effective energy eigenvalues obtained by measuring the wavelengths of these oscillations are listed for comparison with those for an isolated atomic column in Table 1. From the discrepancy between the value for an isolated atomic column and an atomic column situated within a crystal, it is clear that

reasonable agreement with a multislice simulation will be obtained only if the channelling eigenvalue is treated in a phenomenological sense as a parameter characterizing the interaction, but not necessarily taken from an exact solution for a completely isolated atomic column. A guide towards the choice of eigenvalues is an empirical linear scaling with the atomic number (Van Dyck & Op de Beeck, 1996). The exact value of E_i may be chosen empirically using a best fit to either multislice (using perhaps a similar structure) or to experimental data.

Using atomic potentials given by Doyle & Turner (1968), atomic coordinates given elsewhere (Sinkler *et al.*, 1998b), and the channelling eigenvalues from multislice calculations, the electron exit wave for $(\text{Ga},\text{In})_2\text{SnO}_5$ in [010] orientation was calculated from Eq. (4) for a number of thicknesses, and is compared with multislice simulations in Figs 3 and 4. The only additional parameters used in the simulations were the accelerating voltage (300 kV) and Debye-Waller factors B which were set equal to 0.3 \AA^2 for the metal atoms and 0.5 \AA^2 for the oxygen atoms for both sets of simulations. Shown in Fig. 3 are comparisons of the moduli $|\psi(\mathbf{R},z)-1|$, while in Fig. 4 the complex $\psi(\mathbf{R},z)-1$ are plotted using an Argand diagram representation. In the latter, the real and imaginary parts of each pixel value in the calculated unit cell are plotted on the horizontal and vertical axes. As can be seen, the $|\psi(\mathbf{R},z)-1|$ tend to remain similar at small thickness, but also change in strongly

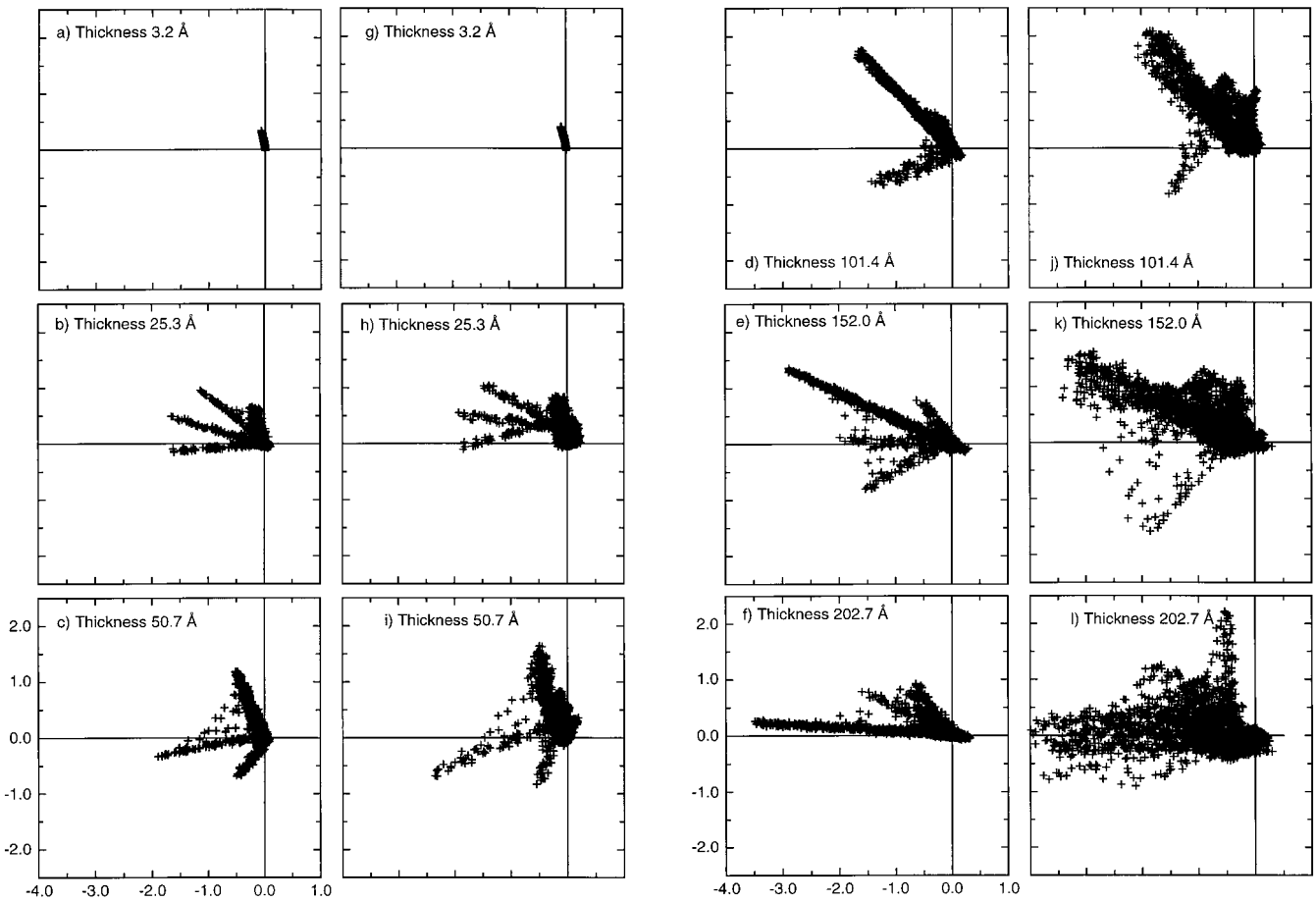


Fig. 4. Comparison of Argand representations of the exit waves $\psi(\mathbf{r})-1$ for $(\text{Ga},\text{In})_2\text{SnO}_5$ calculated using Eq. (4) (a–f) and multislice (g–l). All values are relative to a unit incident beam amplitude. Scaling on all graphs is identical.

parallel ways as the thickness increases. The similarities persist in spite of the appearance of ring-like 2s states centred on the heavier cation positions in the multislice calculations at thicknesses beyond 50 Å. An additional feature which is reproduced well using Eq. (4) is the predominance of the light atoms in the waves starting at thicknesses of ≈ 50 Å. This feature is explainable by the channelling eigenvalue in the denominator of each atomic term in (4), which counteracts and actually reverses the larger potentials of the heavier metal cations (Sinkler *et al.* 1998a). For thicknesses beyond 100 Å, the agreement becomes merely qualitative, and in particular it is noted that the peaks at the atomic positions in the multislice simulations have a tendency to broaden significantly in comparison with the form of the atomic potential (Sinkler & Marks, 1999).

A final comparison between the exit waves calculated using the channelling approximation and multislice is the scaling of the Fourier coefficients, which is shown in Fig. 5. This is of particular importance for structure refinements using electron diffraction intensities. As can be seen from the figure, the approximation of Eq. (4) does a significantly

better job than a simple kinematical approximation in matching the intensities predicted by a multislice calculation to thicknesses at which a kinematical approximation is no longer justifiable. In general, the failure of the kinematical approximation to reproduce the Fourier amplitudes becomes pronounced at thicknesses for which the change in $|\psi(\mathbf{r})-1|$ deviates significantly from linear. From Fig. 2, this occurs in the present case for the tin atoms at a thickness of ≈ 30 Å, and in agreement, the scaling between $|\Psi(\mathbf{h})|$ and the kinematical structure factors $|F(\mathbf{h})|$ breaks down between 25 Å and 50 Å. The successful incorporation of dynamical effects in the Fourier amplitudes of the exit wave is seen in the continued rough scaling between the multislice $|\Psi(\mathbf{h})|$ and that from the channelling theory for a thickness of 50 Å, which from Fig. 2 is already beyond first oscillation period for the tin atoms.

4. Application of channelling to HREM image contrast

Imaging aberrations can be modelled in the linear imaging approximation by multiplying the wave's Fourier transform

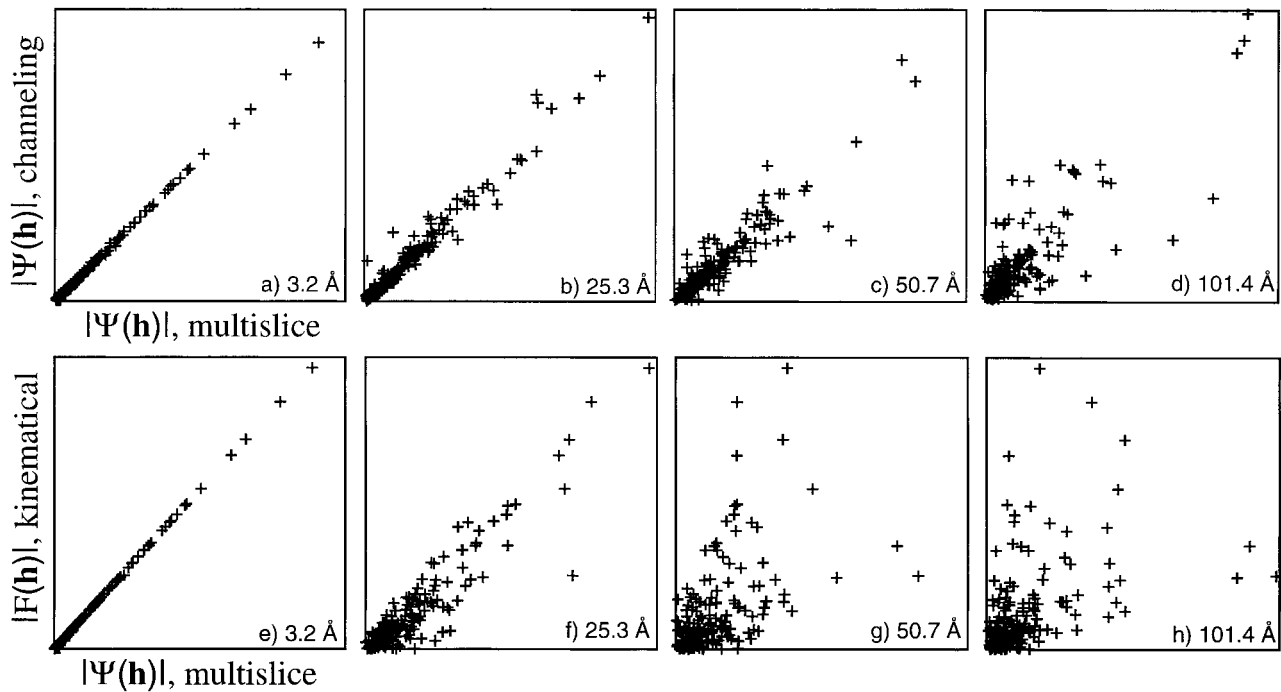


Fig. 5. a-d. Examination of scaling between Fourier moduli $|\Psi(\mathbf{h})|$ of the exit wave for $(\text{Ga}, \text{In})_2\text{SnO}_5$ calculated using Eq. (6), and that calculated using multislice. Thicknesses are indicated in the Figures. e-h. For comparison, the corresponding scaling of the kinematical structure factors $|F(\mathbf{h})|$ with the $|\Psi(\mathbf{h})|$ from multislice is shown.

by the incoherent envelope and coherent transfer function $E(\mathbf{u})$ and $\exp(-i\chi(\mathbf{u}))$, resulting in:

$$\Psi'(\mathbf{u}, t) = \delta(\mathbf{u}) + \sum_i \frac{\tilde{V}_i(\mathbf{u})}{E_i} E(\mathbf{u}) \exp(i[2\pi i \mathbf{u} \cdot \mathbf{R}_i - \chi(\mathbf{u})]) \\ \times \left(\exp\left(-i\pi \frac{E_i}{E_0} kt\right) - 1 \right) \quad (6)$$

in which the $\tilde{V}_i(\mathbf{u})$ are the Fourier transforms of the atomic column potentials, and the parameter t replaces z as the specimen thickness. The image Fourier transform is given in the linear imaging approximation (Self & O'Keefe, 1988) as:

$$I(\mathbf{u}, t) = \Psi'(\mathbf{u}, t) + \Psi'^*(-\mathbf{u}, t) \quad (\text{for } \mathbf{u} \neq 0) \quad (7)$$

Neglecting asymmetric aberrations (primarily astigmatism and beam tilt), the image Fourier transform from (6) and (7) is given by:

$$I(\mathbf{u}, t) = 4 \sum_i \frac{\tilde{V}_i(\mathbf{u})}{E_i} \sin(\pi K_i t) \exp(2\pi i \mathbf{u} \cdot \mathbf{R}_i) \\ \times E(\mathbf{u}) \sin(\chi(\mathbf{u}) - \pi K_i t) \quad (\text{for } \mathbf{u} \neq 0) \quad (8)$$

where $K_i = (-E_i/2E_0)k$ is the inverse of the channelling oscillation period (E_i is taken to be negative for bound states). From Eq. (8), it can be seen that the inclusion of dynamical effects via the channelling approximation leads to a modification of the standard $\sin(\chi)$ expression for weak

phase objects (see for instance Spence, 1988) to include a thickness component. In addition, the contrast level has a species-dependent modulation with thickness due to the $\sin(\pi K_i t)$ term.

From (8), it should thus be expected that optimum imaging conditions will depend not merely on defocus and optical parameters but also on specimen thickness and the nature of the specimen. The transfer of contrast from a given atomic column is controlled from (8) by an effective contrast transfer function (dynamical contrast transfer function, or D-CTF) given by $\sin(\pi K_i t) E(\mathbf{u}) \sin(\chi(\mathbf{u}) - \pi K_i t)$, depending both on the phase $\pi K_i t$, and defocus Δz . A tableau representing the D-CTF is shown in Fig. 6. The leftmost column of Fig. 6 approximately represents the classical kinematical CTF. Strictly considered, the latter is obtained when the term $\pi K_i t$ is equal to $n\pi$, in which case there is zero contrast in the present model. For small values of $\pi K_i t$, optimum defocus conditions occur near to the classical Scherzer defocus $\sqrt{(C_s \lambda)}$, at -420 \AA in the present case, for which the transfer function has a broad negative pass band. However, as can be seen from Fig. 6, the overall contrast level improves when the phase $\pi K_i t$ is near to $\pi/2$, and with increasing phase there is a shift in the optimum pass band toward smaller defocus values.

The D-CTF presented in Fig. 6 permits far more accurate detailed insight into HREM image contrast than does the kinematical CTF, as can be illustrated using the

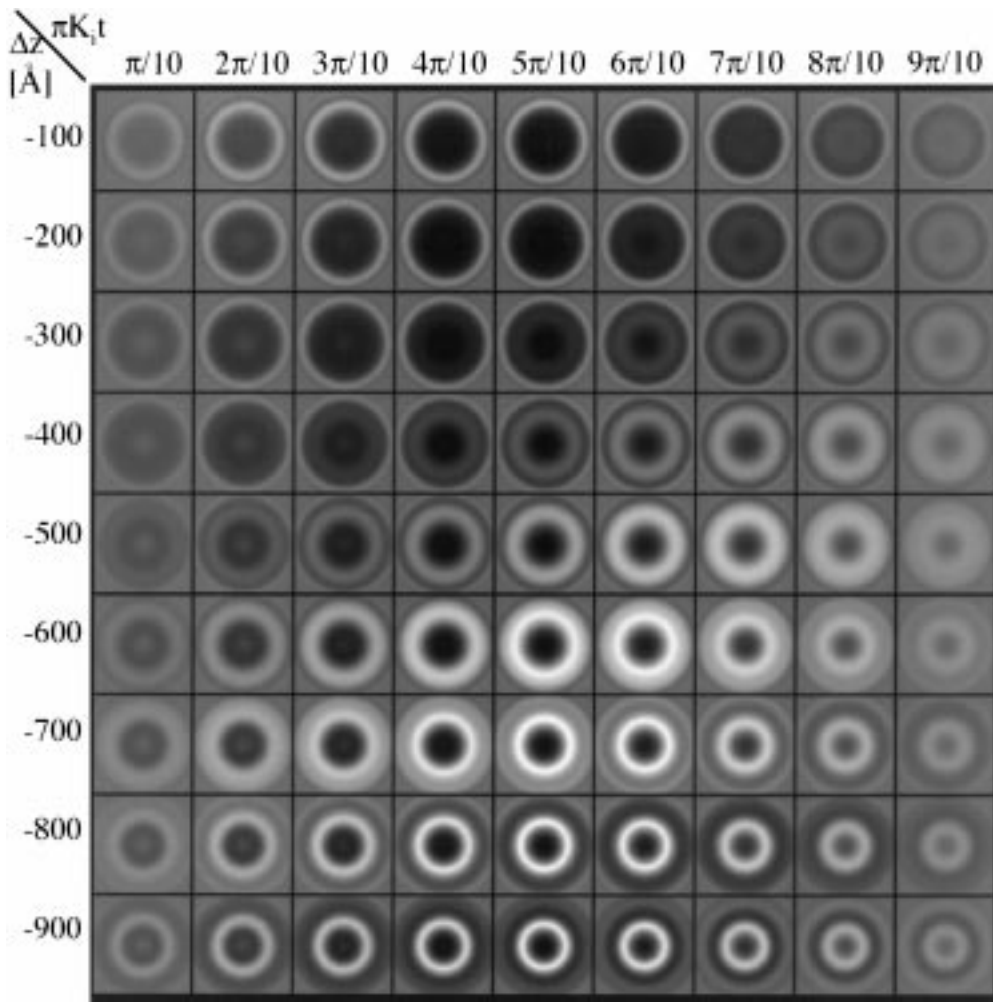


Fig. 6. Tableau showing the dynamical CTF (D-CTF) $\sin(\pi K_i t) \sin(\chi(u) - \pi K_i t)$, calculated for values of defocus Δz and $\pi K_i t$ which are noted. The scaling is such that the edge of each box corresponds to $|u| = 0.5625 \text{ Å}^{-1}$. The D-CTFs were calculated using a defocus spread of 80 Å , beam convergence of 0.75 mrad , $C_s = 0.9 \text{ mm}$, and zero values for all other image aberrations.

$(\text{Ga},\text{In})_2\text{SnO}_5$ case as an example. Figure 7(a) shows a simulated HREM image along $[010]$ for a thickness of 31.6 Å and defocus of -300 Å (for additional conditions see figure caption). In the figure, the atom positions are indicated, and the atom types can be found by reference to Fig. 1. In Fig. 7(b)–(e) are shown line plots of the D-CTF for each atom of the structure at the same defocus using values of $\pi K_i t$ based on the thickness and the channelling eigenvalues (column 2 of Table 1). From the D-CTF plots, one would expect the oxygen atoms to be weak (due to their small value of $\pi K_i t$ at this relatively small thickness), while all cations should be imaged with negative contrast (i.e. as convex features), in agreement with the simulated image. This is similar to a Scherzer defocus image under roughly kinematical conditions, but is correctly predicted by the D-CTF to occur at a slightly smaller defocus value. The D-CTFs can account for fine details of the image. For example, the gallium D-CTF has the most pronounced pass

band, which explains why it is more strongly imaged than tin or gallium/indium positions, for which the D-CTFs have shallower pass bands. Figure 8 shows a simulated image at -600 Å defocus and 63.3 Å thickness. In this case, the gallium shows strong positive contrast, in agreement with the well-defined positive pass band for gallium in the D-CTF. The tin D-CTF shows negative contrast at low spatial frequency, which explains the dark contrast at the locations of the tin atoms (for which $2s$ states are important at thicknesses in excess of 50 Å , see Fig. 3). The Ga/In positions have an intermediate contrast level, in agreement with their nearly flat D-CTF, and the oxygen atoms tend to have a slight negative contrast. Finally, at -800 Å defocus and 124.5 Å thickness, the predominant feature of the simulated image in Fig. 9(a) is the positive intensity at the oxygen atomic positions. It should be recalled that the particular emphasis of the oxygens is also due to their larger channelling eigenfunctions, as shown in the previous

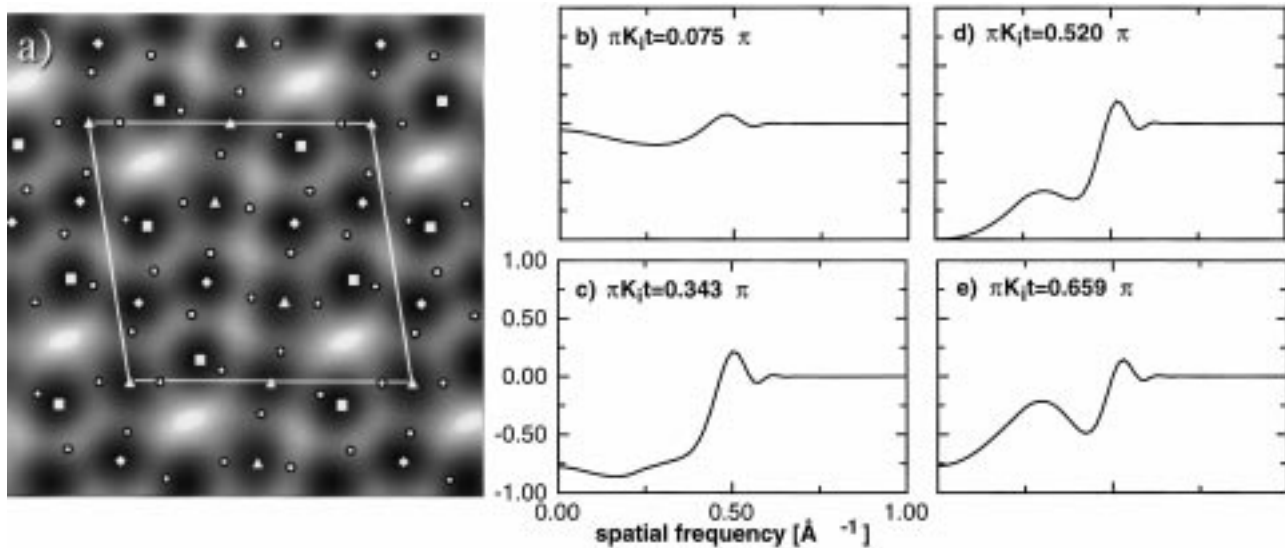


Fig. 7. (a) Multislice calculation of HREM image of $(\text{Ga},\text{In})_2\text{SnO}_5$ at -300\AA defocus and 31.63\AA thickness. Additional imaging parameters are as in Fig. 6, in addition to which a 0.5\AA gaussian smearing in the image has been applied to simulate specimen vibration. Atomic positions are indicated in the figure using \bullet = oxygen, \blacksquare = gallium, $=$ gallium-indium and \blacktriangle = tin. b–e show D-CTFs for (b) oxygen, (c) gallium, (d) gallium-indium, (e) tin, which were calculated using the thickness and imaging parameters, as well as effective channelling eigenvalues from dynamical exit wave calculations (Table 1, column 2).

section. The galliums, which should appear bright as well, are somewhat obscured by the nearby oxygen atoms, and the tins are present as broad dark features in the image, in agreement with the narrow negative pass band in the D-CTF plot.

As the thickness increases, the strengths of diffracted beams increase to become comparable to that of the direct beam, resulting in a breakdown in the linear imaging

approximation. An additional term needs to be added to $I(\mathbf{u})$, $P(\mathbf{u})$ given by

$$P(\mathbf{u}) = 4 \sum_{i,j} A_i(t) A_j^*(t) \int \tilde{V}_j(\mathbf{v} - \mathbf{u}) \exp[-2\pi i(\mathbf{v} - \mathbf{u})\mathbf{R}_j + i\chi(\mathbf{v} - \mathbf{u})] \tilde{V}_i(\mathbf{v}) \exp[2\pi i\mathbf{R}_i\mathbf{v} - i\chi(\mathbf{v})] E(\mathbf{v}, \mathbf{v} - \mathbf{u}) d\mathbf{v} \quad (9)$$

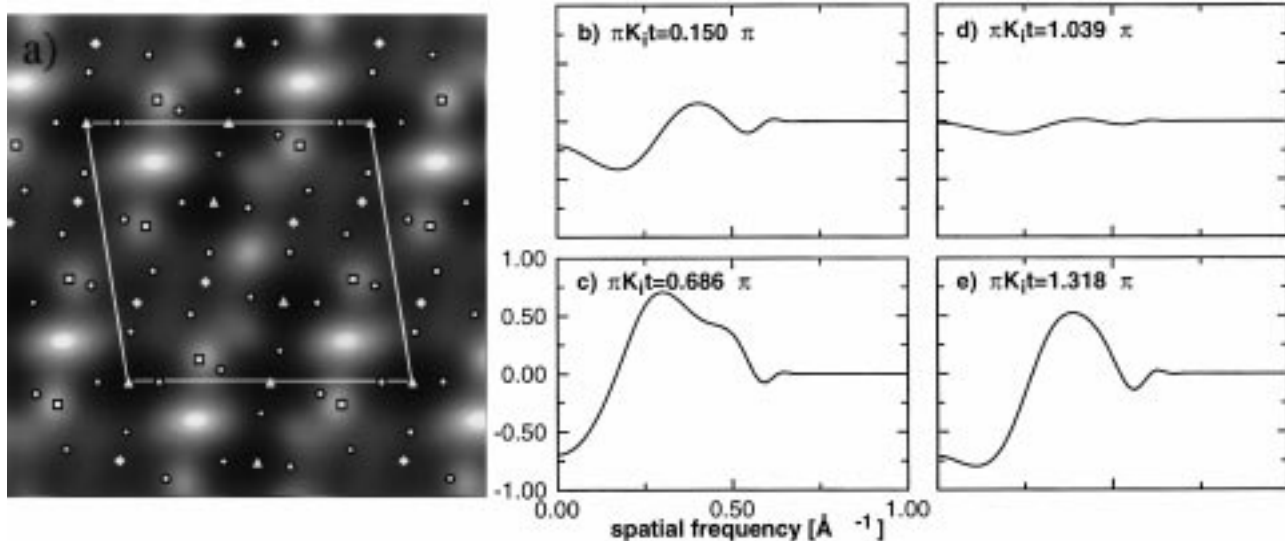


Fig. 8. (a) Calculated HREM image as in Fig. 7a, but for -600\AA defocus and 63.26\AA thickness. b–e show D-CTFs for the same conditions for (b) oxygen, (c) gallium, (d) gallium-indium, (e) tin.

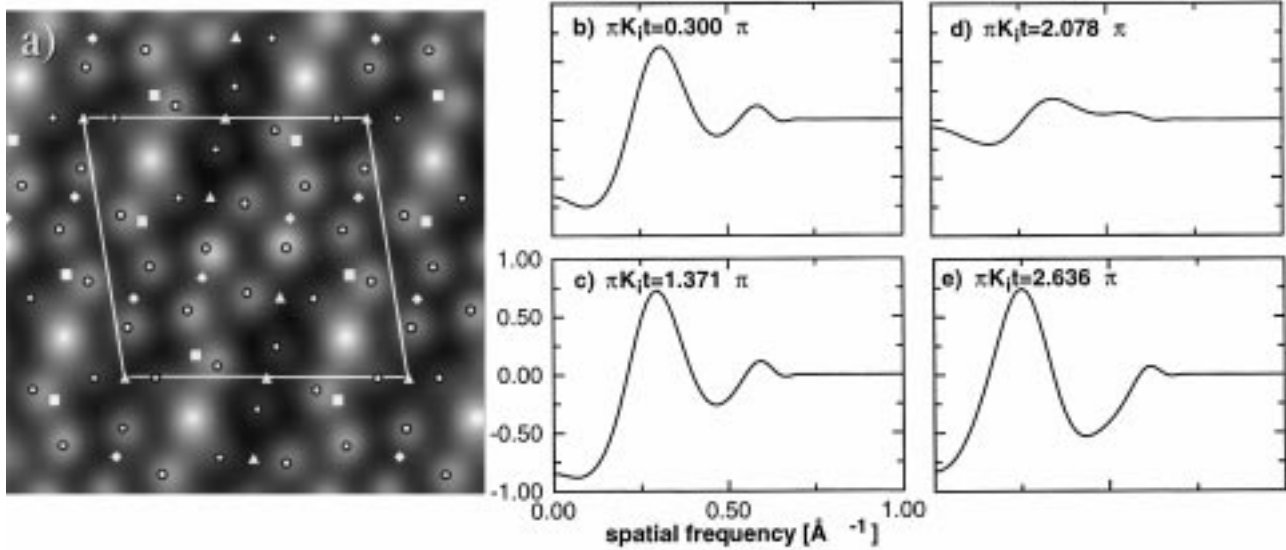


Fig. 9. (a) Calculated HREM image as in Fig. 7a, but for -800 \AA defocus and 126.53 \AA thickness. b–e show D-CTFs for the same conditions for (b) oxygen, (c) gallium, (d) gallium-indium, (e) tin.

where

$$A_i(t) = \frac{\sin(\pi K_i t)}{E_i} \exp(i\pi K_i t) \quad (10)$$

With the exception of the envelope term $E(\mathbf{v}, \mathbf{v} - \mathbf{u})$, the integral in (9) is similar in form to a convolution between two functions $A_j^*(\mathbf{u})$ and $A_i(\mathbf{u})$, in which $A_i(\mathbf{u})$ is the Fourier transform of $V(\mathbf{R} - \mathbf{R}_i)^* T(\mathbf{R})$, and $T(\mathbf{R})$ is the point spread function, the Fourier transform of $\exp(-i\chi(\mathbf{u}))$. If there is little overlap in the potentials of the atomic columns at R_i and R_j , and if the point spread function is sufficiently localized, the integral will be small. For structures in which

there is little overlap between neighbouring atomic column potentials, this is the case to a first approximation for all $i \neq j$, and Eq. (9) can be rewritten:

$$P(\mathbf{u}) = 4 \sum_i |A_i|^2 \exp(2\pi i \mathbf{u} \cdot \mathbf{R}_i) \int [\tilde{V}_i(\mathbf{v} - \mathbf{u}) \tilde{V}_i(\mathbf{v}) \exp[i\chi(\mathbf{v} - \mathbf{u}) - i\chi(\mathbf{v})] E(\mathbf{v}, \mathbf{v} - \mathbf{u}) d\mathbf{v} \quad (11)$$

In conventional non-linear theory (Bonevich & Marks, 1988), the envelope function is expressed as a product of two gaussians describing the contrast effects of beam convergence and defocus spread. Both of these gaussians

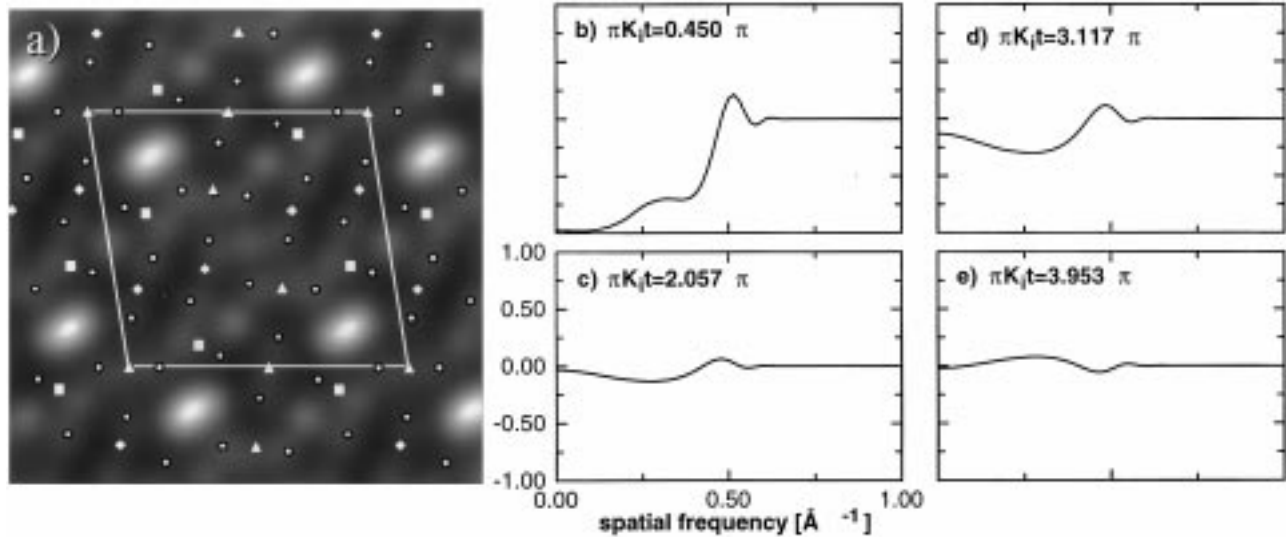


Fig. 10. (a) Calculated HREM image as in Fig. 7a, but for -300 \AA defocus and 189.8 \AA thickness. b–e show D-CTFs for the same conditions for (b) oxygen, (c) gallium, (d) gallium-indium, (e) tin.

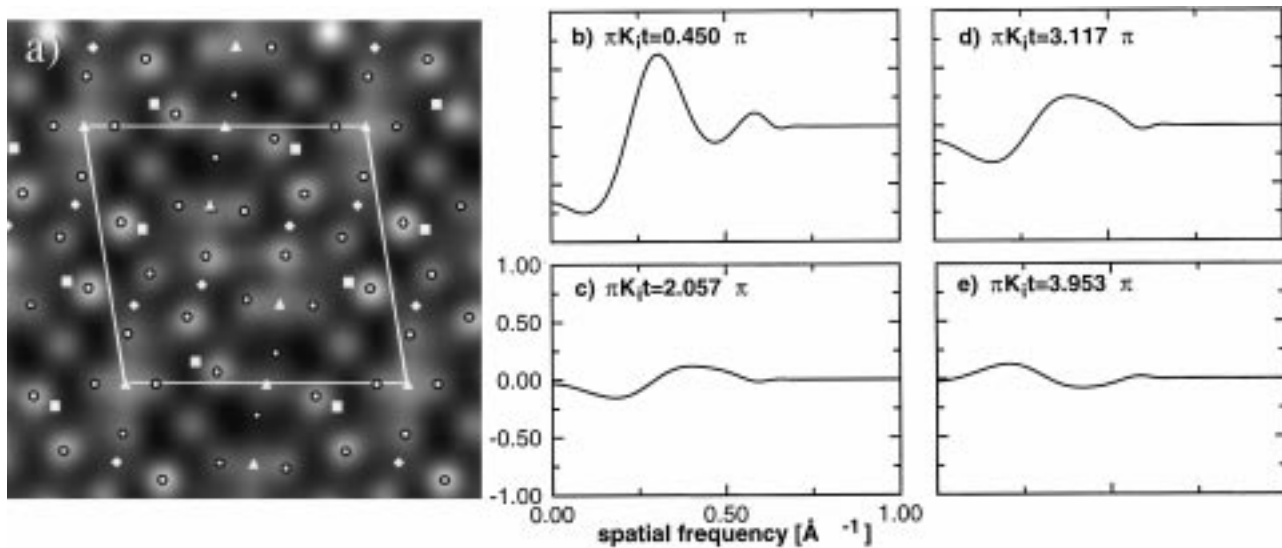


Fig. 11. (a) Calculated HREM image as in Fig. 7a, but for -700 \AA defocus and 189.8 \AA thickness. a–e show D-CTFs for the same conditions for (b) oxygen, (c) gallium, (d) gallium-indium, (e) tin.

are maximal when $|\mathbf{v}| = |\mathbf{v} - \mathbf{u}|$, and therefore, a rough approximation of non-linear effects is simply:

$$P(\mathbf{u}) = 4 \sum_i |A_i|^2 \exp(2\pi i u R_i) \int \tilde{V}_i(\mathbf{u})^2 d\mathbf{u} \quad (12)$$

This corresponds in real space to positive features at the atomic columns, scaled by a thickness-dependent factor $|A_i|^2$, and by the square of the atomic potential. The approximation may be used as a guide to interpretation of a small non-linear correction at moderate thickness.

Figures 10 and 11 show examples of images at 189.8 \AA thickness and -300 \AA and -700 \AA defocus, respectively. Because the thickness is constant between the two images, the only change in the D-CTFs is due to the defocus change. In Fig. 10, all D-CTFs except that for oxygen are relatively small, due to the phase factors for the cations, which are all reasonably close to an integer multiple of π . The oxygen has a broad negative pass band, and yet it can be seen at several positions in the figure that there are faint concave (positive) contrast features at the oxygen positions. This is consistent with the approximate analysis of non-linear imaging effects given above, and is explainable by a cancellation of the negative features predicted using linear theory by the positive contribution of the non-linear cancellation term. Finally, at 700 \AA defocus, Fig. 11 shows strongly positive features at the oxygen atomic positions, which in this case result from a reinforcement of the linear and non-linear effects.

5. Discussion

In the present work, simple expressions have been developed using channelling theory for both the electron exit wave and HREM image intensity. Of most immediate value to

interpretation of microscopical data is the insight into HREM image interpretation which can be obtained by a reasonably simple analytical combination of channelling and linear imaging theories. From the examples shown in the last section, the D-CTF can explain HREM image contrast in most significant details, where clearly the use of a single kinematical CTF would be insufficient. The D-CTF is valid throughout the thickness regime used for most HRTEM imaging applications in inorganic chemistry and materials science, and its validity in the thicker part of this regime can be extended by using a simple approximation to non-linear effects. The most significant limitation to application of the present theory is in the assumption of non-overlapping atomic column potentials. However, a parallel approach using the more general channelling expression Eq. (1) may be useful for more arbitrary structures.

In addition to application to HREM imaging, the channelling approach to diffraction calculation has already been shown to provide a full explanation of direct methods results using dynamical diffraction intensities. The possibility of using direct methods with dynamical diffraction intensities relies on the ability to formulate an expected form for the exit wave, much as classical direct methods rely on the expectation of a real-space electron density distribution consistent with the presence of atoms. Electron channelling theory provides an approximate form which is suitable for dynamical direct methods. In particular, Eq. (4) predicts an exit wave with atom-like maxima each with a relatively constant phase. Therefore, electron channelling is central to development of techniques using quantitative electron diffraction measurements to solve crystal structures.

Finally, the present work has explored the possibilities and limitations of electron channelling theory as a basis for quantitative structure refinements using electron diffraction measurements. As is clear from Fig. 5, the channelling theory permits rapid calculation of intensities in reasonable agreement with dynamical calculations for limited thicknesses. Use of the theory in a refinement scheme would require, in addition to atom position data, refinement of the effective value of the phase $\pi K_i t$ for each atomic column position. The speed of such refinements may make them suitable for distinguishing rapidly between a number of crystal structure models.

Acknowledgement

Funding from the National Science Foundation, Science and Technology Center for Superconductivity (DMR 91-20000) is gratefully acknowledged.

References

- Berry, M.V. (1971). Diffraction in crystals at high energies. *J. Physics C*, **4**, 697–722.
- Bethe, H. (1928). Theorie der Beugung von Elektronen an Kristallen. *Ann. Phys.* **87**, 55–129.
- Bonevich, J.E. & Marks, L.D. (1988). Contrast transfer theory for non-linear imaging. *Ultramicroscopy*, **26**, 313–320.
- Cowley, J.M. & Moodie, A.F. (1957). The scattering of electrons by atoms and crystals. I. A new theoretical approach. *Acta Crystallog.* **A34**, 609–619.
- Doyle, P.A. & Turner, P.S. (1968). Relativistic Hartree–Fock X-ray and electron scattering factors. *Acta Crystallog.* **A24**, 390–397.
- Edwards, D.D. & Mason, T.O. (1998). Subsolidus phase relationships in the Ga_2O_3 – In_2O_3 – SnO_2 system. *J. Am. Ceram. Soc.* **81**, 3285–3292.
- Fujimoto, F. (1978). Periodicity of crystal structure images in electron microscopy with crystal thickness. *Phys. Status Solidi*, **45**, 99–106.
- Gemmell, D.S. (1974). Channelling and related effects in the motion of charged particles through crystals. *Rev. Mod. Phys.* **46**, 129–227.
- Howie, A. & Whelan, M.J. (1961). Diffraction contrast of electron microscope images of crystal lattice defects. *Proceedings of the Royal Society (London)*, **A263**, 217–237.
- Kambe, K. (1982). Visualization of Bloch waves of high energy electrons in high resolution electron microscopy. *Ultramicroscopy*, **10**, 223–228.
- Kambe, K., Lehmpfuhl, G. & Fujimoto, F. (1974). Interpretation of electron channeling by the dynamical theory of electron diffraction. *Z. Naturforsch.* **29a**, 1034–1044.
- Lindhard, J. (1964). Motion of swift charged particles as influenced by strings of atoms in crystals. *Phys. Lett.* **12**, 126–128.
- Marks, L.D. (1985) Image localization. *Ultramicroscopy*, **18**, 33–38.
- Ohtsuki, Y.H. (1983). *Charged Beam Interaction with Solids*. Taylor and Francis Inc., New York.
- Scherzer, O. (1949). The theoretical resolution limit of the electron microscope. *J. Appl. Phys.* **20**, 20–29.
- Self, P.G. & O'Keefe, M.A. (1988) Calculation of diffraction patterns and images for fast electrons. *High Resolution Transmission Electron Microscopy and Associated Techniques* (eds P. R. Buseck, J. M. Cowley and L. Eyring), pp. 244–307. Oxford University Press, New York.
- Sinkler, W., Bengu, E. & Marks, L.D. (1998a). Application of direct methods to dynamical electron diffraction data for solving bulk crystal structures. *Acta Cryst.* **A54**, 591–605.
- Sinkler, W. & Marks, L.D. (1999) Dynamical direct methods for everyone. *Ultramicroscopy*, **75**, 251–268.
- Sinkler, W., Marks, L.D., Edwards, D.D., Mason, T.O., Poeppelmeier, K.R., Hu, Z. & Jorgensen, J.D. (1998b). Determination of oxygen atomic positions in a Ga–In–Sn–O ceramic using direct methods and electron diffraction. *J. Solid State Chem.* **136**, 145–149.
- Spence, J.C.H. (1988). *Experimental High-Resolution Electron Microscopy*. Oxford University Press, Oxford. pp. 72–74.
- Sturkey, L. (1962). The calculation of electron diffraction intensities. *Proc. Phys. Soc.* **80**, 321–354.
- Tamura, A. & Ohtsuki, Y.H. (1974). Quantum mechanical study of rosette motion channeling. *Phys. Status Solidi*, **62**, 477–480.
- Van Dyck, D. (1985). *Advances in Electronics and Electron Physics*, **65** (ed. by P. Hawkes), pp. 295–355. Academic Press, New York.
- Van Dyck, D. & Coene, W. (1984). The real space method for dynamical electron diffraction calculations in high resolution electron microscopy I. Principles of the method. *Ultramicroscopy*, **15**, 29–40.
- Van Dyck, D. & Op de Beeck, M. (1996). A simple intuitive theory for electron diffraction. *Ultramicroscopy*, **64**, 99–107.

Note added in proof. J. Hu and M. Tanaka have recently and independently developed expressions for HREM image contrast using the channelling approximation for the electron exit wave. Their work has been submitted to the journal *Ultramicroscopy*.